Development of Human Skin Equivalents with Inducible Ceramide Depletion for In Vitro Modeling of Lipid Impairment

Durotimi O. Dina[1], Miriam Maiellaro[2], Emanuela Camera[2] and John T. Connelly[1]

JID Innovations (2025);**5:**100383 doi:10.1016/j.xjidi.2025.100383

The lipid composition of the epidermis plays a critical role in the skin's barrier function, and defects in lipid synthesis or assembly can cause a spectrum of skin diseases, ranging from dry skin to severe ichthyoses. The aim of this study was to develop an in vitro model of human skin with tunable inhibition of lipid synthesis. Human N/TERT keratinocytes were engineered to express doxycycline-inducible short hairpin RNAs targeting ceramide synthase 3, which is essential for synthesis of ultralong-chain ceramides and skin barrier function. We show that 3-dimensional human skin equivalents with induced knockdown of ceramide synthase 3 display normal stratification and terminal differentiation but have reduced Nile red staining for polar lipids. Further analysis of the lipidome by mass spectrometry confirmed a significant reduction in specific classes of ceramides and ceramide chain length in the ceramide synthase 3–depleted human skin equivalents. We also show that ceramide synthase 3 knockdown is reversible upon removal of doxycycline and can be used to study recovery and repair of epidermal lipids. Together, these findings provide an overall strategy for genetically regulating the lipid composition within human skin models and establish a tunable in vitro model of ceramide deficiency.

Keywords: 3D model, Barrier function, Ceramide, CERS3, Lipidomics, Skin

INTRODUCTION

The skin is a critical first line of defence against pathogens, physical/chemical damage, and UVR, and the uppermost layer of the epidermis, the stratum corneum, forms a selectively permeable barrier that is crucial for the skin's protective function (Nemes and Steinert, 1999). The stratum corneum relies on an intricate network of proteins and lipids, including the lipid lamellar bilayer (LLB) and cornified lipid envelope (Feingold and Elias, 2014). The LLB confers the water-impermeable properties of the epidermis, and the cornified lipid envelope acts as a sealant for the cohesion of the corneocytes and a scaffold for the LLB (Akiyama, 2017; Elias et al, 2014; Nemes and Steinert, 1999; Van Smeden et al, 2014; Wertz et al, 1989). These lipid-based structures consist of ceramides, cholesterol, and fatty acids, with ceramides making up the greatest fraction by mass (Kendall et al, 2017).

The specific class of ω-esterified ultralong-chain ceramides, also known as the acylceramides (acylCers), are key for the molecular organization and subsequent function of the LLB and cornified lipid envelope, and the enzyme ceramide synthase 3 (CerS3) is uniquely required for acylCer synthesis (Kihara, 2016; Rabionet et al, 2014). To date, 5 species of ω-esterified hydroxy ceramides have been identified: Cer[EOH], Cer[EOP], Cer[EOS], Cer[EODS], and Cer[EOSD]. Their unique chemical structure, namely their esterification to linoleic acid, is responsible for the formation and organization of the LLB (Behne et al, 2000; Breiden and Sandhoff, 2014). Both Cer[EOS] and Cer[EOH] play important roles in the long-periodicity-phase lamellar organization of the LLB, and it has been shown that in the absence of Cer[EOS], almost no long periodicity phase is formed (Bouwstra et al, 2001, 2000, 1998). Overall deficiencies in ceramides can compromise the barrier function of the skin and contribute to numerous skin conditions, ranging from dry skin to severe ichthyoses (Coderch et al, 2003; Sahle et al, 2015; Schreiner et al, 2000; Shen et al, 2018), and long-periodicity-phase malformation directly correlates with an inadequate epidermal barrier and a dry skin phenotype (Bouwstra et al, 2002; Imokawa et al, 1991; Schreiner et al, 2000).

CerS3 deficiency in mice leads to a loss of ultralong-chain ceramides and subsequent fatality shortly after birth (Jennemann et al, 2012). Variation in the *CERS3* gene in humans affect barrier function and can cause specific forms of autosomal recessive congenital ichthyoses (Elias et al, 1984; Oji et al, 2010). For example, the codon exchange variant (p.Trp15Arg) results in moderate lamellar ichthyosis

[1]*Centre for Cell Biology and Cutaneous Research, Faculty of Medicine and Dentistry, Queen Mary University of London, London, United Kingdom;* and [2]*Laboratory of Cutaneous Physiopathology and Integrated Center of Metabolomics Research, San Gallicano Dermatological Institute, IRCCS, Rome, Italy*

Correspondence: John T. Connelly, Centre for Cell Biology and Cutaneous Research, Faculty of Medicine and Dentistry, Queen Mary University of London, 4 Newark Street, London E1 2AT, United Kingdom. E-mail: j.connelly@qmul.ac.uk

Abbreviations: 2D, 2-dimensional; 3D, 3-dimensional; acylCer, acylceramide; CerS3, ceramide synthase 3; ddH_2O, double-distilled water; Dox, doxycycline; HSE, human skin equivalent; KD, knockdown; LLB, lipid lamellar bilayer; NTC, nontargeting control; shRNA, short hairpin RNA

Received 9 January 2025; revised 11 April 2025; accepted 29 April 2025; accepted manuscript published online XXX; corrected proof published online XXX

Cite this article as: JID Innovations 2025;5:100383

with a reduction in long-chain acylCers (Eckl et al, 2013), and similar findings have been reported for other variants leading to Cers3 deficiency (Radner et al, 2013). Thus, Cers3 and acylCers appear to be crucial for the lipid barrier function of the skin.

Human skin equivalents (HSEs) that replicate the 3-dimensional (3D) structure and function of the skin in vitro are powerful tools for investigating human-specific disease mechanisms and, in a few cases, have been applied to lipid-associated diseases. For example, HSEs constructed using patient-derived keratinocytes have been used to replicate disease phenotypes of CerS3 deficiency in autosomal recessive congenital ichthyoses (Eckl et al, 2013). HSEs have also been used to model harlequin ichthyosis using keratinocytes with engineered knock out of the lipid transporter ABCA12 (Enjalbert et al, 2020). Importantly, HSEs are also compatible with lipidomic analysis through mass spectrometry (Thakoersing et al, 2013) and can be used to replicate key differences in the lipid composition of the epidermis in diseases, such as atopic dermatitis (Danso et al, 2017). However, despite these advances and the importance of lipids in the skin barrier, there are limited experimental models that support precise modulation of lipid synthesis.

Because lipid deficiencies can cause a spectrum of conditions with varying degrees of severity, the ability to precisely tune the amount and composition of lipids within an HSE model would be advantageous for in vitro modeling of human lipid disorders and testing drugs and skincare products. In this study, we developed an inducible HSE model of ceramide deficiency using engineered keratinocytes with doxycycline (Dox)-inducible knockdown (KD) of CerS3. We focused on CerS3 as a proof of concept because it is a critical regulator of ceramide synthesis in the epidermis and is solely responsible for the synthesis of the acylCer class of lipids. We show that reduction of CerS3 expression in keratinocytes results in a global depletion of polar lipids within the epidermis of the HSE as well as a lower abundance of specific classes of ceramides and a reduction in ceramide chain length. Moreover, we demonstrate the reversibility of inducible CerS3 KD and ability to study the kinetics of lipid recovery within the HSEs after acute ceramide depletion. Together, these findings establish a robust and tunable methodology for modeling lipid impairment in human skin.

RESULTS

Establishment of HSEs with inducible CerS3 KD

To develop an in vitro human skin model with tunable control of epidermal lipids, we constructed HSEs using keratinocytes with inducible depletion of ceramides, which are essential for maintaining skin moisture and barrier integrity (Akiyama, 2017; Breiden and Sandhoff, 2014; Elias et al, 2014). N/TERT keratinocytes were engineered to stably express short hairpin RNAs (shRNAs) targeting *CERS3* under the control of a Dox-inducible promoter (Baron and Bujard, 2000; Loew et al, 2010; Zhou et al, 2006), alongside expression of RFP (Figure 1a). HSEs were constructed by embedding primary dermal fibroblasts in a hydrogel derived from decellularized extracellular matrix of porcine skin (Sarmin and Connelly, 2022), and engineered keratinocytes expressing *CERS3* targeting or nontargeting control (NTC)

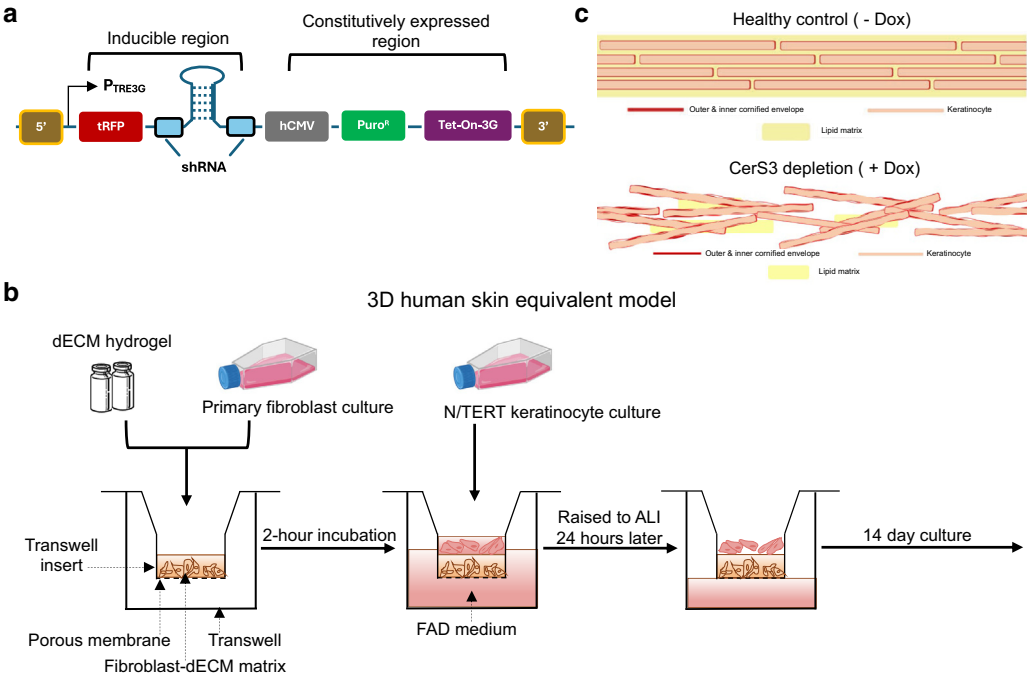

Figure 1. Development of HSEs with inducible CerS3 knockdown. (**a**) Schematic of the shRNA lentiviral construct (SMARTvector, Horizon Discovery). The constitutively expressed region under the control of the human cytomegalovirus promoter included elements for expression of the Tet-On-3D transactivator and puromycin resistance, whereas the inducible region contained the shRNA element and tRFP reporter under the control of the TRE3G promoter that is activated by Dox. (**b**) Schematic overview of the process for constructing 3D dECM HSEs at the ALI of Transwell inserts. (**c**) Schematic of expected disruption of epidermal lipids after addition of Dox (+Dox) and knockdown of CerS3. 3D, 3-dimensional; ALI, air–liquid interface; CerS3, ceramide synthase 3; dECM, decellularized extracellular matrix; Dox, doxycycline; HSE, human skin equivalent; shRNA, short hairpin RNA.

shRNAs were seeded on the surface. HSEs were cultured at the air–liquid interface for 14 days to induce epidermal differentiation and stratification (Figure 1b), and through the addition of Dox to the culture medium, we aimed to induce CerS3 depletion and disruption of the lipid barrier (Figure 1c).

Analysis of RFP expression in 2-dimensional (2D) culture first confirmed inducible transgene activation in transduced cells. Maximal RFP expression was reached within 3 days of treatment with a minimum of 0.1 mg/ml of Dox, which was then used for all subsequent experiments (Figure 2a). In all 4 cell lines, over 90% of cells were RFP positive after Dox treatment, whereas RFP expression was negligible in the absence of Dox (Figure 2b). RT-qPCR analysis indicated significant *CERS3* downregulation with Dox exposure in the sh1 and sh2 lines but not in the NTC and sh3 lines (Figure 2c), and a similar KD was observed at the protein level by western blotting (Figure 2d). Because the sh3 line showed no effective KD of CerS3, it was excluded from further analysis.

We next assessed CerS3 KD in 3D HSE models. We confirmed RFP transgene activation through the full thickness of the epidermal layer in the Dox-treated cultures (Figure 2e). In accordance with the 2D data, a significant reduction in the CerS3 protein was observed for sh1 and sh2 HSEs treated with Dox compared with untreated controls but not for the NTC HSEs (Figure 2f). With these results, we confirmed KD

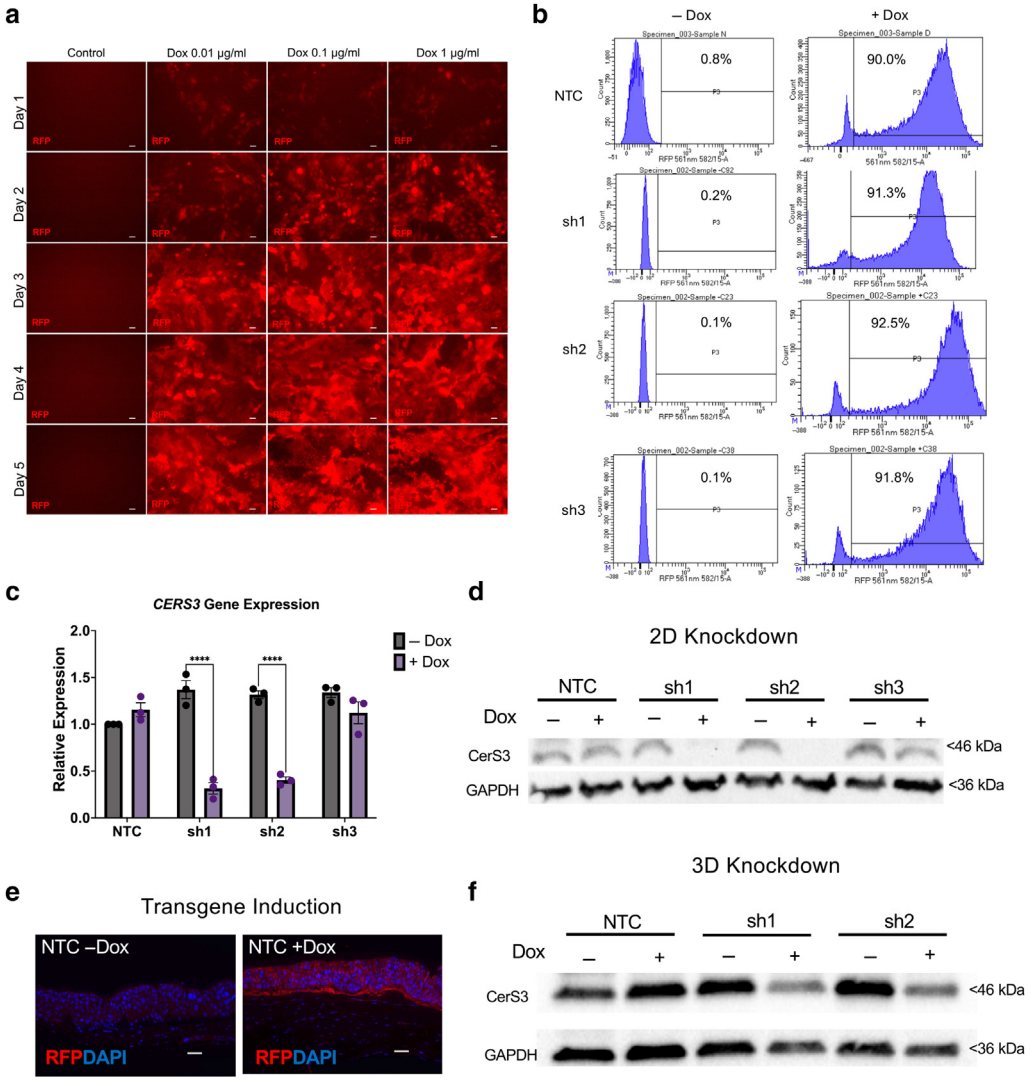

Figure 2. Characterization of CerS3 knockdown in 2D and 3D culture. (**a**) RFP fluorescence imaging in N/TERT keratinocytes transduced with NTC shRNA and treated with 0, 0.01, 0.1, or 1 µg/ml of Dox for a period of 6 days. Images are representative of n = 3 experiments. Bar = 50 µm. (**b**) Flow cytometry for RFP reporter expression across NTC and shRNA knockdown cell lines (sh1, sh2, and sh3) in 2D culture without or with 0.1 µg/ml Dox treatment for 7 days. Percentage of RFP-positive cells are noted for each condition. (**c**) Analysis of *CERS3* knockdown in 2D culture by RT-qPCR. Data represent fold change in expression ($2^{-\Delta\Delta Ct}$ method) relative to that of GAPDH and untreated NTC cells for the shRNA-transduced N/TERT lines without or with Dox treatment (0.1 mg/ml) for 7 days. Data are presented as mean ± SEM. ****$P < .0001$ with 2-way ANOVA and Tukey's multiple comparison test. n = 3 experiments. (**d**) Representative western blot for CerS3 and GAPDH expression for all cell lines in 2D culture without or with Dox treatment for 7 days. (**e**) Immunofluorescence staining for the inducible tRFP reporter (red) in HSEs constructed with NTC keratinocytes without or with Dox treatment for 14 days. Bar = 50 µm. (**f**) Representative western blot for CerS3 and GAPDH in HSEs constructed with NTC, sh1, and sh2 cell lines and cultured without or with Dox for 14 days. 2D, 2-dimensional; 3D, 3-dimensional; CerS3, ceramide synthase 3; Dox, doxycycline; HSE, human skin equivalent; NTC, nontargeting control; shRNA, short hairpin RNA.

efficacy and the ability to inducibly deplete CerS3 within the 3D HSE model using 2 different shRNA constructs: sh1 and sh2.

CerS3 depletion reduces polar lipid content in HSEs independently of epidermal differentiation and stratification

To determine the effects of CerS3 depletion in the HSE constructs, we first examined overall changes in epidermal structure and terminal differentiation. H&E staining indicated no apparent differences in stratification or cornification in the Dox-treated sh1 and sh2 models compared with that in their untreated controls or NTC models (Figure 3a). Likewise, there were no differences in epidermal thickness between any of the conditions (Figure 3b). Immunofluorescence staining for transglutaminase-1 and loricrin also revealed no discernible differences in the expression of late terminal differentiation proteins (Figure 3c and d).

Nile red was then used to detect the levels of nonpolar and polar lipids in the epidermal layer (Fowler and Greenspan, 1985; Sheu et al, 2003). Staining for both polar and nonpolar lipids was greatest in the stratum corneum in all models (Figure 4a and b). Although the level of nonpolar lipids was not altered in response to CerS3 depletion, we observed a significant reduction in the levels of polar lipids for the Dox-treated sh2 HSEs, and there was a small but nonsignificant reduction in polar lipids in the Dox-treated sh1 HSEs (Figure 4a and b). Together, these results suggest that induced CerS3 depletion within the HSE model disrupts the polar lipid composition of the stratum corneum independently of keratinocyte terminal differentiation.

CerS3 depletion disrupts the ceramide lipid composition of the HSEs

Although Nile red staining suggested that the lipid composition was perturbed in the CerS3-depleted HSEs, further analysis was required to determine the molecular-level changes in the lipidome. We therefore performed liquid chromatography and mass spectrometry analysis to profile the lipid composition of the HSEs with CerS3 depletion. Overall, liquid chromatography and mass spectrometry identified 263 known lipid species across all HSE samples. To assess the similarity between the HSE model and human skin, we compared the proportions of different ceramide classes (Figure 5a) in the epidermis of our control (NTC) HSEs with those in the epidermis of normal human skin samples. The molar fraction percentage of Cer[NH], Cer[NDS], Cer[AH], Cer[AP], and Cer[ADS] in the HSEs were within 5% of those in the donor skin samples (Figure 5b). The levels of Cer[NP] were 15% lower in the HSE model than in the human skin, whereas Cer[AS] and Cer[NS] were 6% and 16.5% higher, respectively. Importantly, Cer[EOS], the most abundant acylCer, was the only acylCer detected in our HSE model at 1% compared with the 2% in human skin (Kováčik et al, 2014). The overall proportions of ceramides in the epidermis of the human skin T'Kindt samples were also similar to previously reported levels (Kendall et al, 2017; Suzuki et al, 2022; T'Kindt et al, 2012). These results therefore confirmed that key epidermal ceramides were present within the HSE model and could be quantitatively analyzed by liquid chromatography and mass spectrometry.

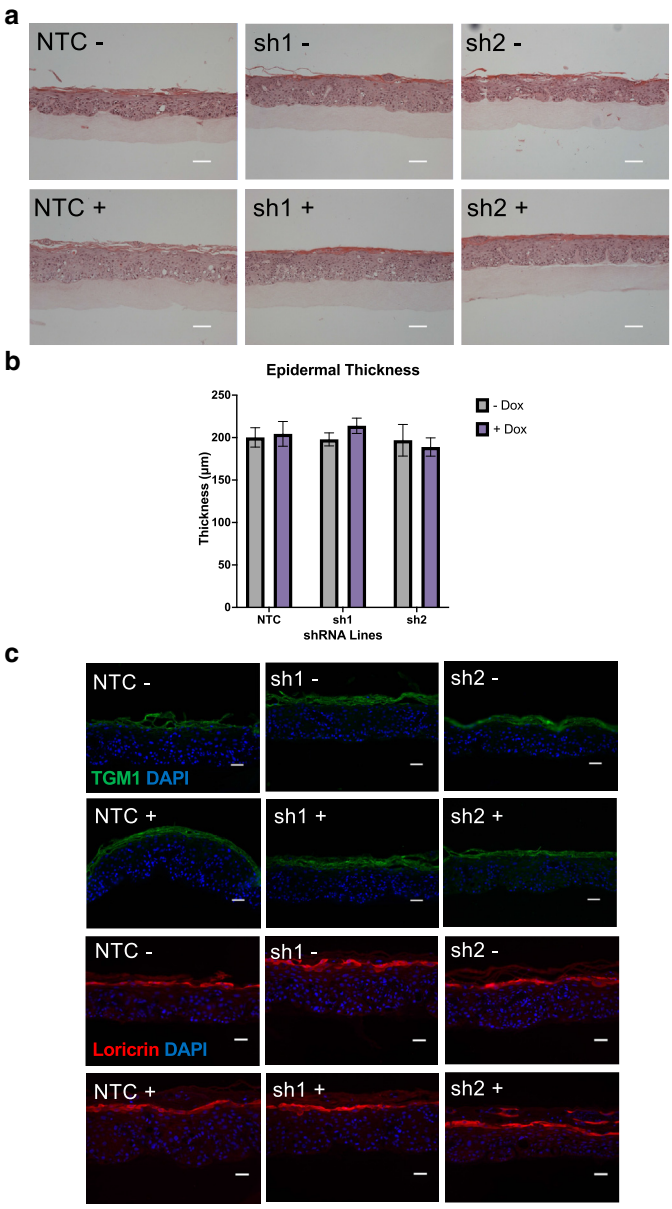

Figure 3. Analysis of stratification and terminal differentiation in 3D HSEs. (**a**) Representative images of H&E staining for HSEs constructed with NTC, sh1, or sh2 keratinocytes without or with Dox treatment (0.1 mg/ml) for 14 days. Bar = 100 μm. (**b**) Quantification of epidermal thicknesses using H&E images from HSEs constructed with NTC, sh1, and sh2 lines and without or with doxycycline treatment for 14 days. Data represent the mean ± SEM of 3 technical replicates, and n = 3 independent experiments. No significant differences were determined by 2-way ANOVA. Immunofluorescence staining for (**c**) TGM1 and (**d**) loricrin, counterstained with DAPI. Bar = 20 μm. 3D, 3-dimensional; Dox, doxycycline; HSE, human skin equivalent; NTC, nontargeting control.

We next examined the effects of CerS3 KD on lipid composition of the HSEs. Hierarchical clustering based on all identified lipids grouped by lipid class revealed distinct patterns of lipid composition, and the Dox-treated sh1 and sh2 samples clustered together and away from the untreated and NTC samples (Figure 5c), indicating a clear effect of CerS3 depletion on the lipid profile of the HSE. CerS3 depletion in both the sh1 and sh2 lines predominantly caused a downregulation of lipids in the HSE model (Figure 6a and b),

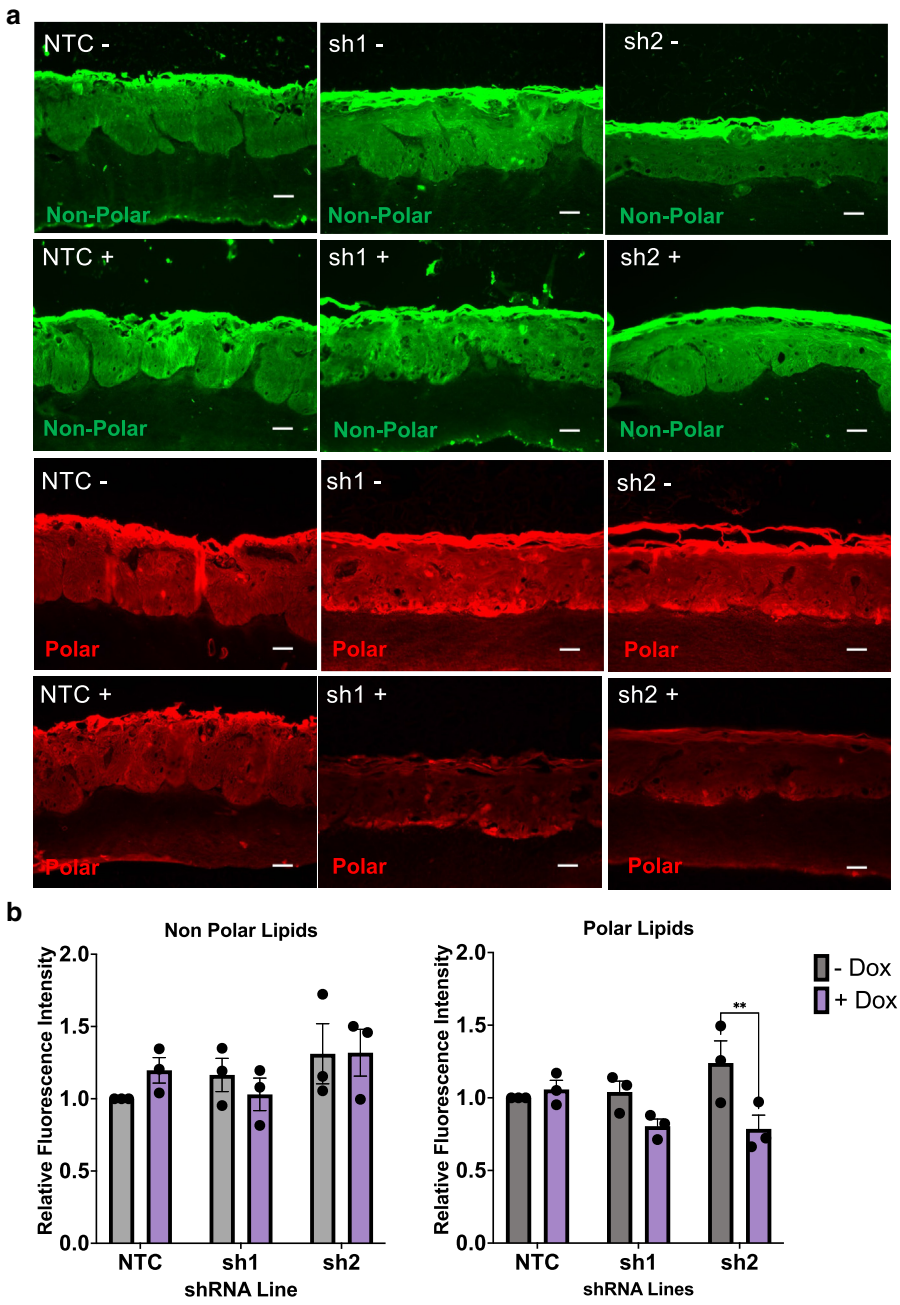

Figure 4. Analysis of lipid content in 3D HSEs. (**a**) Representative images of nonpolar (green) and polar (red) lipid staining using Nile red, for HSEs constructed with NTC, sh1, or sh2 keratinocytes without or with Dox treatment (0.1 mg/ml) for 14 days. Bar = 50 μm. (**b**) Quantification of Nile red fluorescence intensity for nonpolar (left panel) and polar (right panel) signals for all cell lines without or with Dox treatment. Data represent the mean ± SEM normalized to the untreated NTC HSEs. $^{**}P < .01$ with 2-way ANOVA and Tukey's multiple comparison test. n = 3 experiments. 3D, 3-dimensional; Dox, doxycycline; HSE, human skin equivalent; NTC, nontargeting control.

consistent with the Nile red staining. On the basis of a significance criterion of $\log_2$ fold change ≥ 1 and a $-\log_{10} P \geq 1.3$, 15 and 3 specific lipid species were significantly downregulated in the Dox-treated sh1 and sh2 models, respectively (Figure 6a and b). In addition to individual lipids, we observed a significant downregulation of the ceramide classes Cer[EOS], Cer[NH], and CER[NP] for sh1 Dox-treated HSEs compared with that for NTC samples and a nonsignificant decrease for sh2 (Figure 7a, c, and d). Linoleic acid (C18:2) is the most common fatty acid used to esterify and create acylCers and is cleaved to form the omega-acylated-hydroxy-ceramides (Breiden and Sandhoff, 2014; Rabionet et al, 2014). Linoleic acid was significantly depleted in the sh1 +Dox group (Figure 7f), which we hypothesize may be a feedback response to the decrease in availability of acylCers. By contrast, there were no significant differences in free fatty acids, cholesterol, or other ceramide classes (Figure 7b and g–p).

Ceramide chain-length distribution plays an important role in barrier mechanics (Danso et al, 2017; Eckl et al, 2013; Ishikawa et al, 2010; Suzuki et al, 2022), and an increase in shorter-chain ceramides leads to a decrease in skin barrier function (Ishikawa et al, 2010; Janssens et al, 2012). Therefore, we next analyzed ceramide chain-length changes within our model. Combining all ceramide classes together, there were significant decreases in longer carbon chain length ceramides (C43 and C44) in both the Dox-treated sh1 and sh2 samples compared with that in NTC samples and in C42 for sh1 (Figure 8a and b). Looking at specific ceramide

a

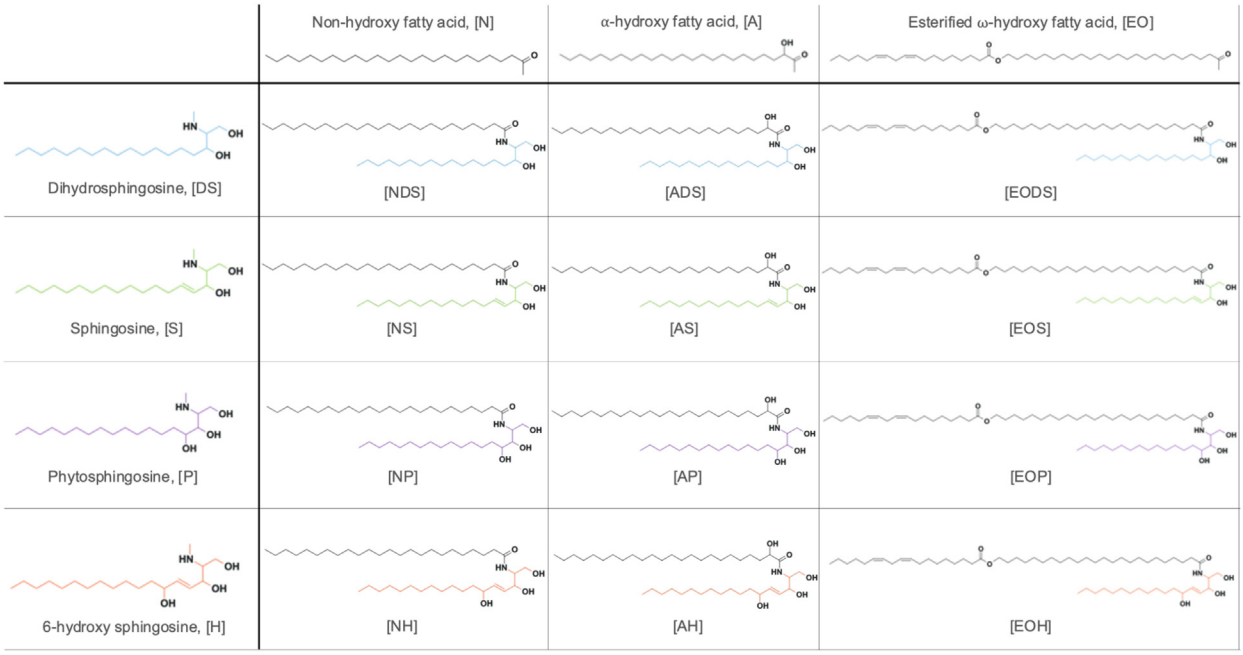

b

Ceramide Class	NP	NH	NDS	AH	AP	EOS	AS	NS	ADS
Skin %	25.0	17.1	16.1	4.7	5.7	2.1	4.6	23.3	1.4
HSE %	9.7	15.1	16.0	1.8	1.3	1.0	10.5	39.8	5.0

c

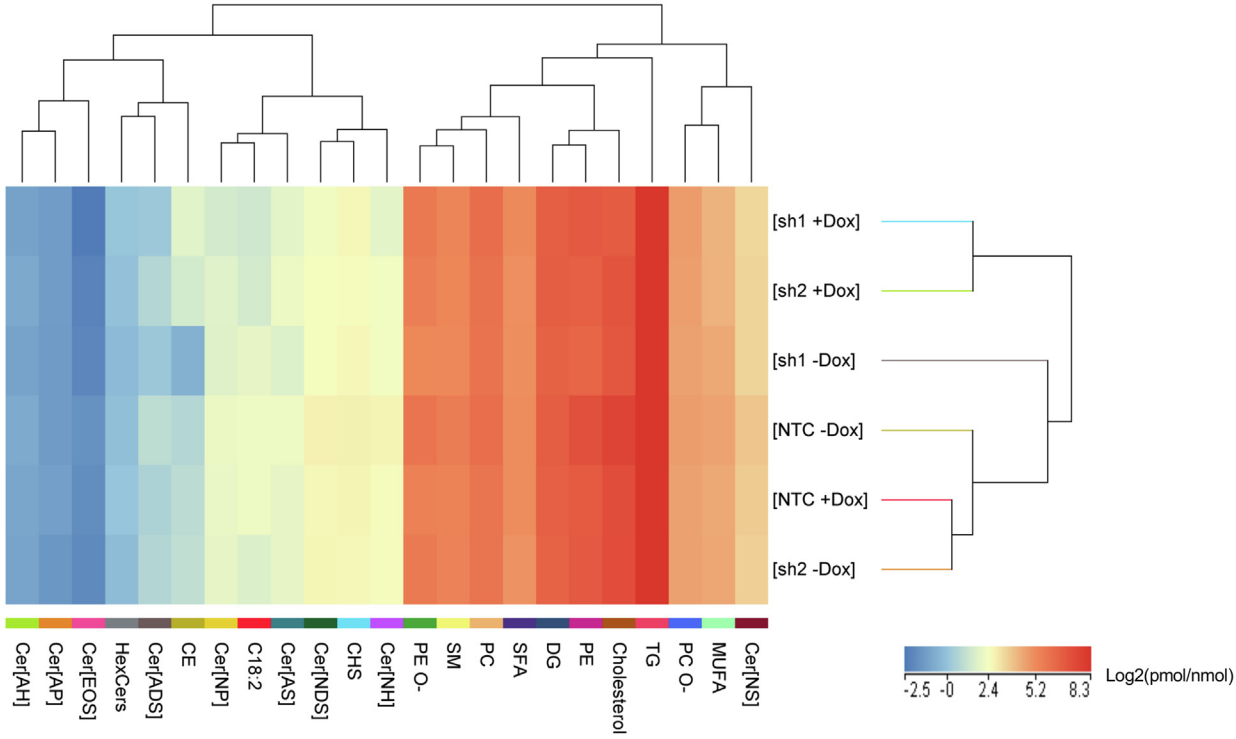

Figure 5. Lipidomic composition and clustering in HSE models. (**a**) Summary of free ceramide structures and naming conventions, adapted from Van Smeden et al (2014). (**b**) Comparison of the percentage of different ceramide classes out of the total ceramide content between the epidermis of human skin and HSE models constructed with NTC keratinocytes. Yellow = within 5% of human skin, red = higher in the HSE, and blue = lower in the HSE. Data represent the mean of n = 3 HSEs from independent experiments. (**c**) Heat map and hierarchical clustering of lipid classes (263 identified lipid species) and experimental conditions, NTC, sh1, and sh2 (without and with doxycycline 0.1 mg/ml), against lipid class groupings of ceramides Cer[NS], Cer[NH, Cer[NDS], Cer[AS], Cer [NP], Cer[ADS], Cer[AP], Cer[AH], Cer[EOS], MUFAs, SFAs, PC, PE, DGs, TGs, cholesterol, SM, CHSs, linoleic acid (C18:2), CEs, and HexCers. n = 3

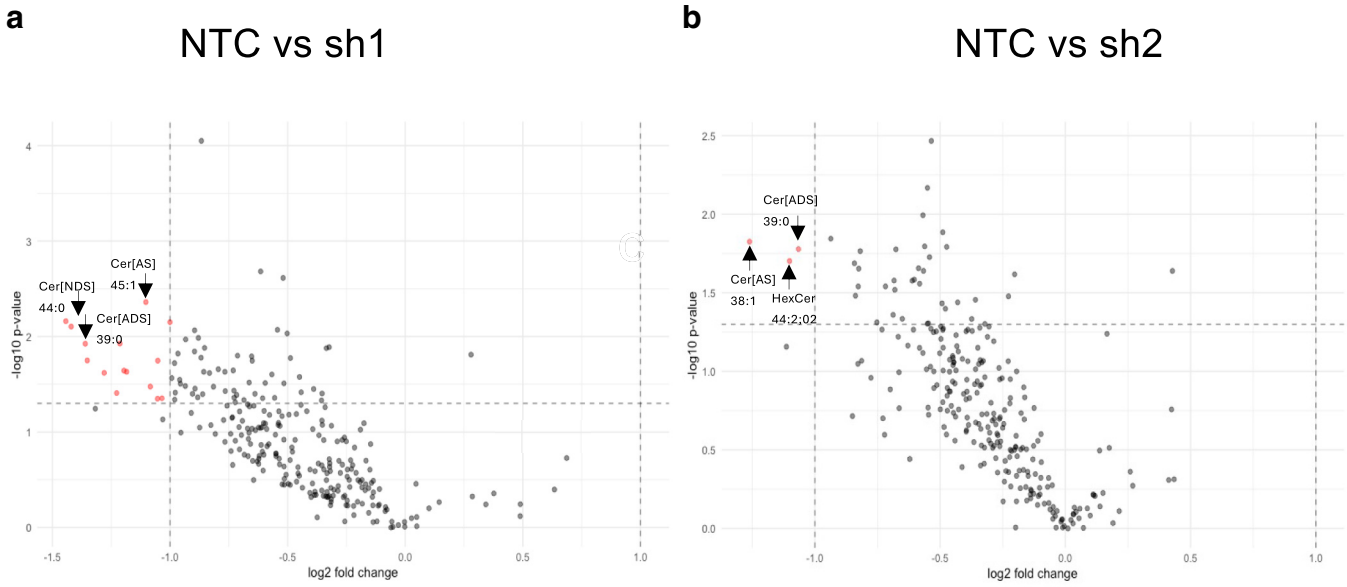

c

sh1			sh2		
Name	log_fc	log_pval	Name	log_fc	log_pval
CER[EOS]48:3	-0.8669099	4.04955461	CER[EOS]48:3	-0.4894265	1.88565765
Cer[AS]45:1	-1.1027074	2.36122596	Cer[AS]38:1	-1.2607122	1.82574866
Cer[NDS]44:0	-1.4429721	2.16075562	Cer[ADS]39:0	-1.0654657	1.77851026
Cer[NDS]46:0	-1.0004292	2.15102875	HexCer 44:2;O2	-1.1013752	1.7023697
Cer[ADS]42:0	-1.4205778	2.10463081	CER[EOS]46:3	-0.5468378	1.30599938
Cer[NP]44:0	-1.2131179	1.92676132	CER[EOS]50:3	-0.4406427	0.92301967
Cer[ADS]39:0	-1.3603067	1.92474685	CER[EOS]66:3	-0.728302	0.70068271
CER[EOS]50:3	-0.6531193	1.79236321			
Cer[NP]43:0	-1.3520561	1.74947157			
Cer[NDS]43:0	-1.0521232	1.74713953			
Cer[NH]44:1	-1.1958156	1.64338986			
Cer[NS]44:1	-1.1845307	1.63119338			
Cer[NS]46:2	-1.2800356	1.61952706			
Cer[NH]42:1	-1.0838053	1.47573371			
Cer[EOS]46:3	-0.8153423	1.47474257			
Cer[AP]48:0	-1.2271936	1.40870687			
Cer[NS]43:1	-1.0345576	1.35339633			
C18:2	-1.0533249	1.34868997			
Cer[EOS]66:3	-1.3178602	1.24467926			

Figure 6. Downregulation of individual lipid species in CerS3 knockdown model. (**a, b**) Volcano plot showing $\log_2$ fold change and $-\log_{10}$ *P*-value (unpaired t-test) for all the annotated lipids detected in the HSE models comparing (**a**) NTC + Dox with sh1 + Dox and (**b**) NTC + Dox with sh2 + Dox. (**c**) Table summary of annotated lipid species, the total carbon chain length of the LCB and FA saturation state. Highlighted in red are those that met the significance criteria, and those that were found in both the sh1 and sh2 knockdown models are highlighted in purple. The acylceramides detected (highlighted in gray) are included even though they did not meet the significance criteria of this analysis. CerS3, ceramide synthase 3; Dox, doxycycline; FA, fatty acid; HSE, human skin equivalent; LCB, long-chain base; NTC, nontargeting control.

classes, Cer[NS] and Cer[NH] showed significant reductions in the ratio of long- to short-chain lipids for the sh1 and sh2 groups compared with that for the NTC (Figure 8c). Together, these findings indicate that CerS3 depletion disrupts the ceramide composition of HSEs, resulting in reduced ceramide content and a shift in the long to short ceramide chain length ratio.

Lipid restoration lags CerS3 protein expression in a model of lipid recovery

A unique feature of the inducible shRNA model is the ability to switch the KD mechanism on and off in a controllable fashion. To further leverage this inducibility, we investigated lipid recovery within the HSE model after restoration of CerS3 expression. Time-course analysis of CerS3 expression in 2D

experiments. Data represent $\log_2$ transformed levels of each lipid class (pmol) relative to total lipid content (nmol). CE, cholesterol ester; CHS, cholesterol sulphate; DG, diglyceride; HexCer, hexosylceramide; HSE, human skin equivalent; MUFA, monounsaturated fatty acid; NTC, nontargeting control; PC, phosphatidyl choline; PE, phosphatidylethanolamine; SFA, saturated fatty acid; SM, sphingomyelin; TG, triglyceride.

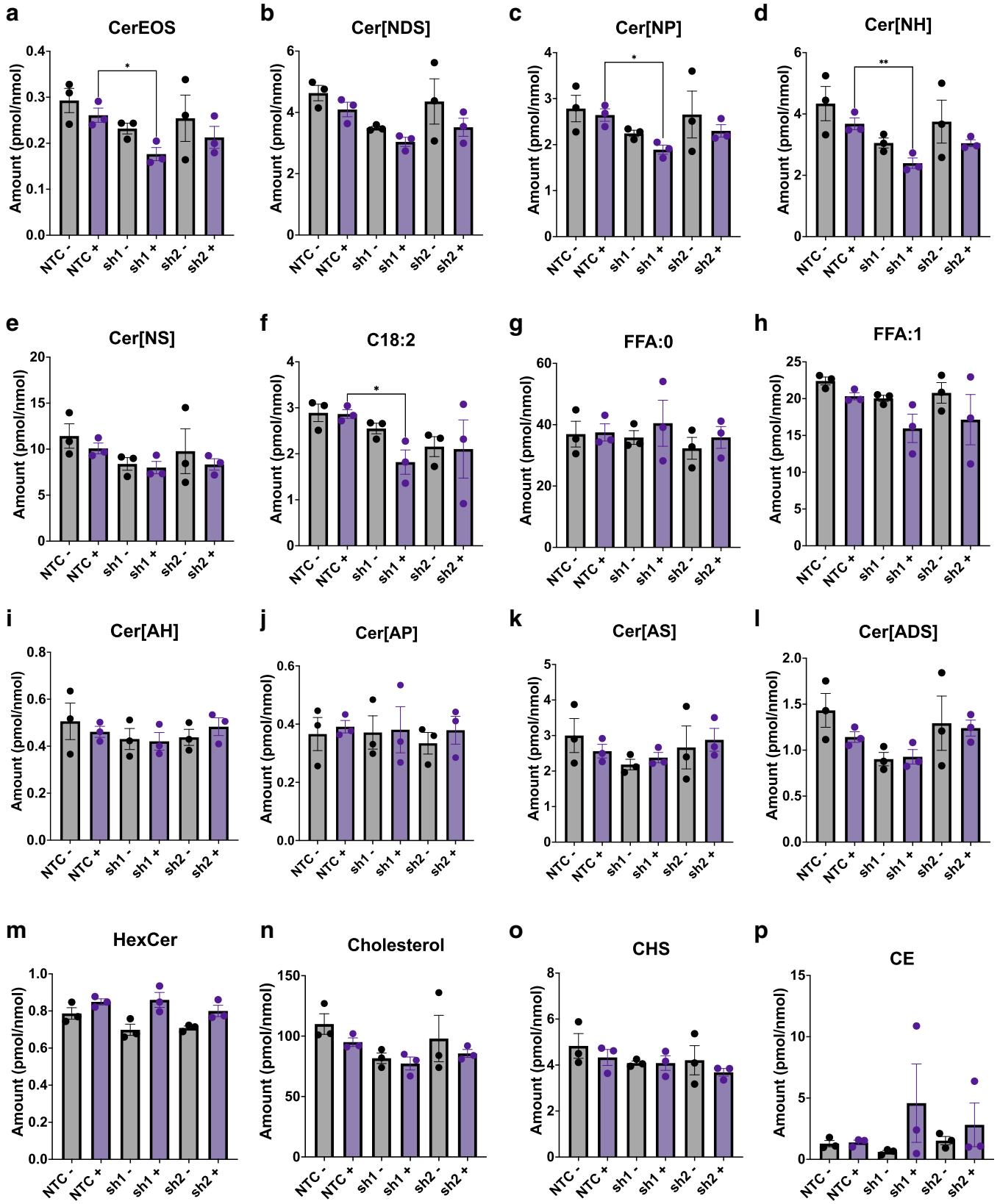

Figure 7. Effects on CerS3 depletion on lipid classes. Analysis of molar lipid content grouped by different classes, including (**a**) Cer[EOS], (**b**) Cer[NDS], (**c**) Cer[NP], (**d**) Cer[NH], (**e**) Cer[NS], (**f**) linoleic acid (C18:2), (**g**) saturated fatty acids (FFA:0), (**h**) monounsaturated fatty acids (FFA:1), (**i**) Cer[AH], (**j**) Cer[AP], (**k**) Cer[AS], (**l**)Cer[ADS], (**m**) HexCer, (**n**) cholesterol, (**o**) CHS, and (**p**) CE. Data are represented as mean ± SEM of pmol of lipid class per nmol of total lipid content. *$P < .05$ with 2-way ANOVA and Tukey's multiple comparison test. n = 3 experiments. CE, cholesterol ester; CerS3, ceramide synthase 3; CHS, cholesterol sulphate; FFA, free fatty acid.

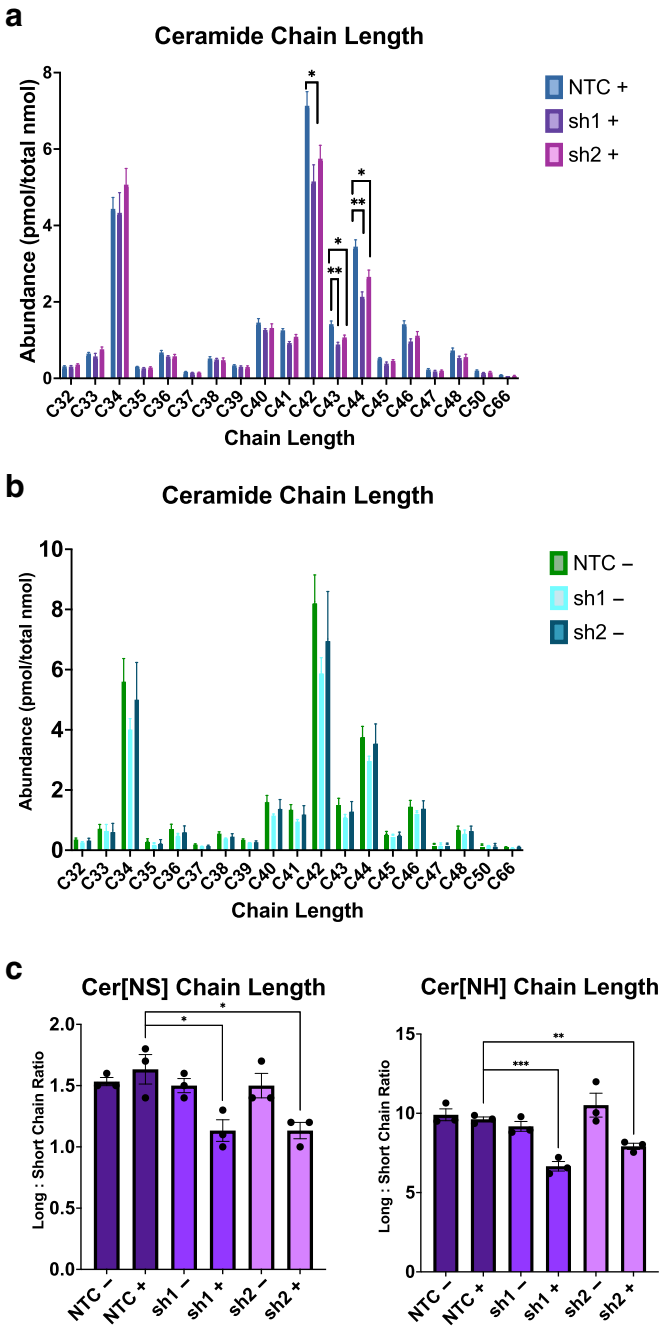

Figure 8. Effects of CerS3 depletion on ceramide chain length in HSE models. (**a**) Analysis of ceramide chain length in Dox-treated NTC, sh1, and sh2 HSEs and (**b**) untreated HSEs. Data represent the abundance of ceramides with 32−66 carbons and are represented as mean ± SEM. $^{**}P < .01$ and $^{*}P < .05$ with 1-way ANOVA with Tukey's multiple comparison test. n = 3 experiments. (**c**) Molar ratio of long-chain ceramides (>40 carbons) to shorter-chain ceramides (<40 carbons) for the most significantly downregulated classes Cer[NS] and Cer[NH]. Data represent the mean ± SEM. $^{*}P < .05$, $^{**}P < .01$, and $^{***}P < .001$ with 2-way ANOVA with Tukey's multiple comparison test. n = 3 experiments. CerS3, ceramide synthase 3; Dox, doxycycline; HSE, human skin equivalent; NTC, nontargeting control.

culture showed that protein levels began to recover within 3 days after Dox removal and were fully recovered within 6 days (Figure 9). We then extended this approach to 3D culture, where CerS3 was depleted for 7 days with the addition

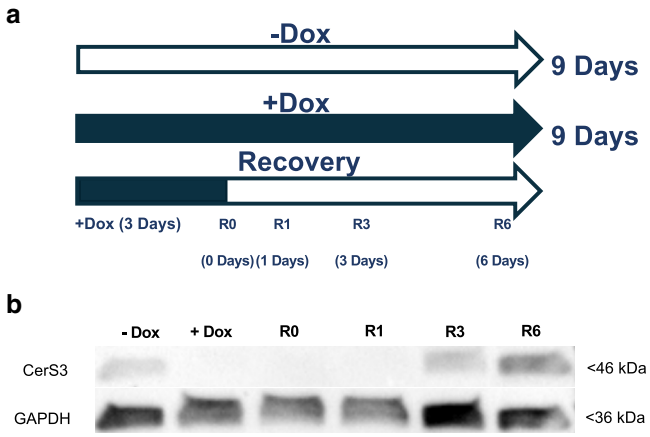

Figure 9. Analysis of CerS3 recovery kinetics in 2D culture. (**a**) The 2D knockdown recovery experiment culture timeline. The experiment consisted of a −Dox and a +Dox condition for 9 days, plus 4 independent recovery conditions where cells were treated with Dox for 3 days followed by sample collection 0, 1, 3, and 6 days after removal of Dox (R0, R1, R3, and R6). (**b**) Representative western blot for CerS3 and GAPDH for the 2 controls and 4 recovery time points. 2D, 2-dimensional; CerS3, ceramide synthase 3; Dox, doxycycline.

of Dox and then allowed to recover for 7 days in the absence of Dox. Lipid content in the recovery model was compared with that in untreated controls or HSEs with CerS3 depletion over the full 14-day culture (Figure 10a). Western blot analysis confirmed a complete recovery of CerS3 at the protein level in both the sh1 and sh2 HSEs compared with that of continuous Dox treatment (62 and 55% Cers3 depletion, respectively) (Figure 10b and c). As before, the polar lipid content was significantly reduced in the sh2 cultures treated with Dox and slightly but not significantly reduced in the sh1-treated cultures. In the sh2 recovery condition, polar lipid content partially recovered to the untreated levels, resulting in nonsignificant differences compared with the continuous CerS3-depleted condition (Figure 10d and e). These results suggest that there is a latent period between recovery of CerS3 protein expression and full restoration of polar lipid content and that 7 days is insufficient for a complete recovery of the lipid composition within the in vitro HSE models. Moreover, these findings demonstrate the utility of HSEs with inducible ceramide depletion for the investigation of lipid barrier damage and repair.

DISCUSSION

In this study, we established and characterized a 3D HSE model with tunable depletion of ceramides through inducible shRNA KD of CerS3. We demonstrate that depletion of CerS3 disrupts the lipid composition of the epidermal layer, including a reduction in distinct classes of ceramides and a shift in ceramide chain-length ratios, consistent with the known roles of CerS3 in the synthesis of ultralong-chain ceramides (Akiyama, 2017; Mizutani et al, 2013; Rabionet et al, 2014). Given that CerS3 levels were not completely knocked down, and there were no observable changes in terminal differentiation, we propose that the model best replicates mild forms of lipid deficiency, such as dry skin. By contrast, total loss of CerS3 is known to cause autosomal

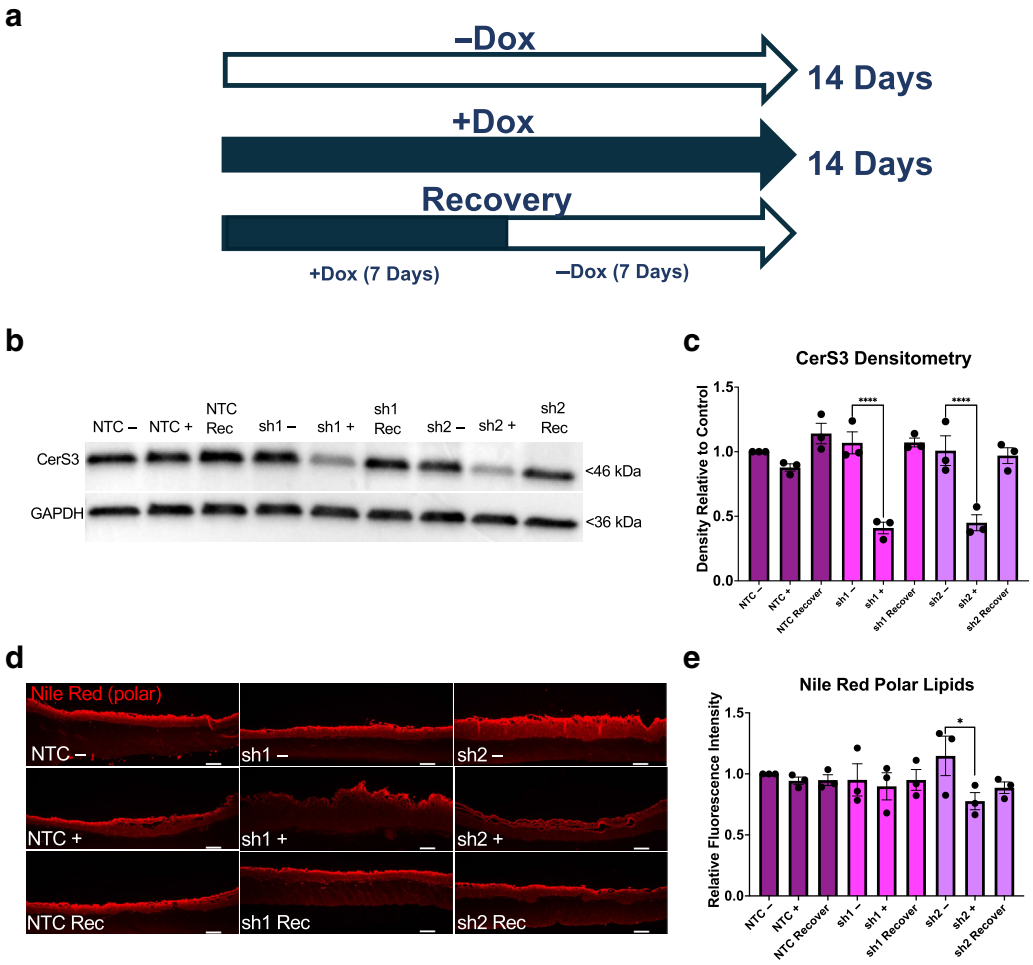

Figure 10. Analysis of CerS3 and lipid restoration in a recovery model. (**a**) Schematic of 14-day experimental timeline for 3D recovery model, including untreated control (14 days −Dox), sustained knockdown (14 days +Dox), and recovery (7 days +Dox followed by 7 days −Dox). (**b**) Representative western blot of CerS3 and GAPDH expression in untreated controls, knockdown, and recovery (denoted as Rec) conditions for NTC, sh1, and sh2 HSEs. (**c**) Quantification of CerS3 protein levels relative to GAPDH and normalized to NTC untreated controls (−Dox). Data are presented as mean ± SEM. ****$P < .0001$ with 2-way ANOVA and Tukey's multiple comparison test. n = 3 experiments. (**d**) Representative fluorescence images of polar lipids detected with Nile red staining in untreated controls, knockdown, and recovery (denoted as Rec) conditions for NTC, sh1, and sh2 HSEs. Bar = 100 μm. (**e**) Quantification of Nile red fluorescence intensity normalized to NTC untreated controls. Data are represented as mean ± SEM. *$P < .05$ with 2-way ANOVA and Tukey's multiple comparison test. n = 3 experiments. 3D, 3-dimensional; CerS3, ceramide synthase 3; Dox, doxycycline; HSE, human skin equivalent; NTC, nontargeting control.

recessive congenital ichthyoses and more severe phenotypes in skin equivalent models (Eckl et al, 2013), suggesting that CerS3 levels correlate with the severity of skin disease. Likewise, CerS3 levels are reduced in atopic dermatitis (Coderch et al, 2003; Danso et al, 2017; Janssens et al, 2012; Sahle et al, 2015). The ability to tune CerS3 levels in vitro may therefore be a useful approach to gaining new insights into its role in skin barrier diseases.

The inducible shRNA strategy employed in this study has several notable advantages for modeling lipid disorders in human skin. The efficient induction of transgene expression in over 90% of cells and lack of leakiness provided tight control over CerS3 expression with Dox and, as demonstrated in the recovery experiments, could be useful for studying kinetics and mechanisms of epidermal barrier repair. It should be noted that although Cers3 protein depletion was observed in both 2D and 3D cultures, the KD was slightly less effective in the 3D model, which may reflect reduced permeation of Dox through the dermal and epidermal layers. Genetic targeting of individual enzymes, such as CerS3, is advantageous for dissecting the role of specific biosynthetic pathways, and this approach could be applied to other ceramide, fatty acid, or cholesterol synthesis pathways in the future. In this study, we also employed engineered immortalized N/TERT keratinocytes, which were advantageous for lentiviral transduction, scale-up, and consistency, while retaining the ability to form well-differentiated HSEs. In future studies, it will be interesting to compare the different effects of CerS3 depletion in HSEs generated with primary keratinocytes, which may display a slightly different lipid profile (Danso et al, 2015; Derr et al, 2019; Reijnders et al, 2015; Van Drongelen et al, 2014). Likewise, an important consideration for future lipid recovery studies will be the role of desquamation, which does not typically occur in vitro but may be required for true regeneration of the epidermis.

Using mass spectrometry, we characterized the specific classes of lipids affected by CerS3 depletion, which caused a downregulation of Cer[NH]; Cer[NP]; and the most abundant acylCer, Cer[EOS], alongside a reduction in ceramide chain lengths. These responses are consistent with the reported changes in ceramide composition for a patient with ichthyosis with *CERS3* sequence variation, with the exception of Cer[NDS], which was nonsignificantly decreased in the current models but increased in patient skin (Yamamoto et al, 2021). These differential effects could potentially be due to different degrees of Cers3 depletion as well as interdonor variability or slight variations in the liquid chromatography and mass spectrometry methodology. Previous studies have also reported a correlation between the [NP]:[NS] ratio and terminal differentiation (Yokose et al, 2020), but given the lack of effects on terminal differentiation in this study, it is not surprising that [NP]:[NS] was similar across all conditions (not shown).

The HSE model and mass spectrometry methods used in this study allowed us to detect 9 of 16 classes of ceramides in roughly similar proportions to the human skin analyzed in this study and in previous studies (Suzuki et al, 2022; T'Kindt et al, 2012). The mass spectrometry analysis focused on freely extractable lipids and, therefore, did not include the 3 protein-bound ceramide classes. Because protein-bound ceramides have previously been shown to be unaffected by *CERS3* alterations (Yamamoto et al, 2021), it is unlikely that they were also affected by CerS3 KD in this study. Importantly, we were able to detect Cer[EOS], but the quantities in the HSE models were slightly lower than in the skin samples. We also did not detect other types of acylCers. These inconsistencies with human skin could reflect limited maturation of the stratum corneum in the HSE model or a lack of sensitivity for detecting low-abundance ceramide classes (Yokose et al, 2020). It should be noted that the mass spectrometry methodology employed in this study used a single internal standard and is therefore only able to measure relative differences in lipid content, and other approaches (Kawana et al, 2020) could be used to determine absolute lipid levels in the future. Although reductions in the abundance of Cer[EOS] were expected on the basis of the known functions of CerS3 (Kihara, 2016; Mizutani et al, 2009; Wegner et al, 2016), the overall effects were relatively modest compared with the level of CerS3 KD, suggesting that even small amounts of CerS3 may be sufficient to generate Cer[EOS]. The reduction in the precursor linoleic acid and ceramides in other biosynthetic pathways also suggests that CerS3 depletion has indirect effects on the ceramide composition of the epidermis. The inducible model may therefore be useful for dissecting crosstalk and feedback mechanisms of ceramide synthesis in future studies.

Of the ceramide classes downregulated in our model system, Cer[NH] and [NP] are also reduced in the skin of patients with atopic dermatitis (Ishikawa et al, 2010). Our model also recapitulated the frequently reported long- to short-chain ceramide shift (Ishikawa et al, 2010; Janssens et al, 2012; Suzuki et al, 2022), including reduced chain length of ceramide subclasses [NS], [NH], [AS], and [AH], which correlated with decreased barrier function in atopic dermatitis (Janssens et al, 2012). Given the reduction in [NS] and [NH] chain lengths observed in this study, it will be interesting in future work to investigate the impacts of CerS3 depletion on barrier function using transepidermal water loss or structural organization of the LLB by small-angle x-ray diffraction (Mieremet et al, 2019; Schreiner et al, 2000; Van Smeden et al, 2014).

In this study, both sh1 and sh2 keratinocyte lines displayed similar levels of CerS3 KD and overall trends in lipid composition with the HSEs. However, polar lipid content was significantly reduced only for sh2, and Cer[EOS], Cer[NH], Cer[NP], and linoleic acid were only significantly reduced for sh1. These differences are likely due to subtle differences in the cell lines, but the overall similarity in the trends and significant differences in chain length indicate that the response is specific to CerS3 and unlikely due to off-target effects of the shRNAs. Although some of the observed changes in lipid composition were less severe than in autosomal recessive congenital ichthyoses, we believe that these smaller effects are still applicable to therapeutic development because many human variants in *CERS3* lead to partial attenuation of protein activity (Yamamoto et al, 2021). Likewise, subtle changes in lipid composition could be relevant for understanding structure–function relationships in conditions such as dry skin and eczema.

Although more work is required to interrogate the effects of CerS3 depletion on nonceramide lipids, our analysis suggested a subtle downregulation in nonceramide species, such as intermediate compounds utilized for lipid biosynthesis. Through a series of reversible reactions, ceramides can be converted into sphingomyelins, glucosylceramides, and phosphorylated signaling species (Kendall et al, 2017; Mullen et al, 2012). Although not significant, we observed decreases in diglycerides and triglycerides, sphingomyelin, and phosphatidylcholine. In addition, sphingomyelins and glucosylceramides are polar species. In de novo ceramide synthesis, ceramides are briefly converted into these polar compounds so they can be transported out of the cell through lamellar bodies before being subsequently hydrolysed back into ceramides. Therefore, a possible hypothesis is that the lack of formation of the original ceramides results in a reduced amount of these polar species being released into the extracellular space, and this contributed to the reduction in fluorescence intensity seen in the Nile red assay.

In summary, the inducible HSE model developed in this study provides a tunable platform in which to modulate and study lipid synthesis in the skin. To our knowledge, this study presents previously unreported in vitro model for selective and reversible ceramide depletion. We propose that these systems will be useful tools for investigating human-specific mechanisms of epidermal barrier function and disease processes. In addition, they have the potential to support animal-free testing of drugs or skincare products for lipid disorders in human skin.

MATERIALS AND METHODS

The 2D monolayer culture

All reagents were from Thermo Fisher Scientific unless otherwise stated. The N/TERT human keratinocyte line was provided by the Rheinwald Lab (Dickson et al, 2000). N/TERTs were cultured at 37 °C and 5% carbon dioxide in FAD medium containing a 1:3

mixture of Ham's F12 and DMEM, supplemented with 1% (v/v) penicillin/streptomycin, 1.8 × 10^{-4} M adenine (Sigma-Aldrich), 10% (v/v) fetal bovine serum (Biosera), 5 μg/ml insulin (Sigma-Aldrich), 0.5 μg/ml hydrocortisone, 10 ng/ml epidermal GF (Peprotech), and 1 × 10^{-10} M cholera toxin (Sigma-Aldrich) and seeded in T75 flasks (6000 cells/cm^2 seeding density). N/TERTs were passaged at 60–70% confluency by rinsing with prewarmed Versene solution followed by incubation with prewarmed 0.25% trypsin-EDTA. Suspension was neutralized with an equal volume of FAD medium before being collected and centrifuged at 200*g* for 5 minutes. Cells were counted and replated at a density of 1 × 10^6 cell per T75 flask.

Primary human fibroblasts were provided by Michael Philpott and obtained from healthy donor abdominal skin (ethical reference number LREC 08/H0704/65). Fibroblasts were seeded at a density of 12,000 cells/cm^2 and cultured at 37 °C and 5% carbon dioxide in DMEM supplemented with 1% penicillin/streptomycin (v/v) and 10% (v/v) fetal bovine serum. Fibroblasts were used up until passage 7.

Decellularized extracellular matrix preparation

For the HSE dermal matrix, we used a decellularized extracellular matrix hydrogel made from pig skin (Sarmin and Connelly, 2022). Fresh pig skin was cut into 1 × 1 cm pieces using scalpels, with as much fat and hair removed by manual scraping. Pieces were soaked in PBS with 1% (v/v) penicillin/streptomycin for 2 hours followed by weighing in sterile tubes. Skin was frozen at −80 °C for 5 hours prior to being freeze dried overnight. Tissue was digested overnight at 4 °C in 560 U/l Dispase (Sigma-Aldrich) solution dissolved in a 10-mM sodium acetate (pH 7.5) and 5-mM calcium acetate buffer solution at 2 ml per gram of tissue to disrupt the epidermal–dermal association. The epidermis was then scraped off using tweezers, and the dermis washed thrice in sterile double-distilled water (ddH_2O) before being washed with constant stirring overnight at room temperature in 70% ethanol. The dermis was then treated with 0.25% Trypsin/0.1% EDTA for 1 hour at 40 °C using a heated plate stirrer. Dermis was again washed in sterile ddH_2O before being incubated at room temperature under constant stirring for 6 hours in a 1% Triton-X, 0.26% EDTA, 0.69% Tris buffer solution. After 6 hours, this solution was replaced with fresh buffer solution, and the dermis was incubated overnight on the magnetic stirrer. The tissue was then washed thrice in sterile ddH_2O, followed by freezing at 80 °C before being freeze-dried overnight. The dried tissue was weighed and digested at 20 mg/ml acidic pepsin solution, which was prepared by dissolving Pepsin A (Sigma-Aldrich) at a final concentration of 1 mg/ml in 0.01 M hydrochloric acid. The dermis was digested at room temperature for 3 days under constant stirring until tissue was fully dissolved. The resulting decellularized extracellular matrix was aliquoted and stored at −20 °C.

The 3D HSE models

HSE models were made in 12-well Transwell plates utilizing 0.4-μm inserts (Merck). Fibroblasts were mixed with thawed aliquots of decellularized extracellular matrix to make a 1 × 10^5 cells/ml suspension, and 340 μl of solution was subsequently pipetted onto the apical side of the Transwell insert. The solution was left to solidify for 2 hours in the incubator. After which, 340 μl of FAD-suspended N/TERTs were added on top of the solidified gel. An additional 340 μl of FAD medium was added to the apical side of the Transwell insert, with a further 500 μl of FAD added to the bottom of the well plate prior to overnight incubation. The following day, the inserts were raised to an air–liquid interface by removing medium from the apical side of the Transwell insert, leaving the top surface of the construct dry. HSEs were maintained at an air–liquid interface for 14 days, with basal media changes conducted every day. From day 7 onward, basal media was supplemented with 50 μg/ml ascorbic acid.

Design and selection of CERS3 shRNA sequences

Three lentiviral inducible SMARTvectors (100 μl, 1 × 10^7 TU/ml) were purchased for the *CERS3* protein coding targets, and the shRNA target sequences were selected from predesigned sequences (Horizon Discovery). For the target gene, 3 KD sequences, named sh1, sh2, and sh3, were all unique because they targeted multiple splice variants, and their alignments with the *CERS3* gene did not overlap. The fourth did not have a targeting nucleotide sequence and was used as a nontargeting control group (NTC). Each construct was transduced into separate N/TERT cell populations, making 4 transduced cell lines in total (Table 1).

KD cell line transduction, selection, and activation

N/TERT cells to be transduced were seeded at a density of 30,000 cells/cm^2 in 6-well plates before incubating in transduction medium with 6 μg/ml polybrene and lentiviral particles at 1.0 multiplicity of infection for 24 hours. Cells were then left to recover in fresh medium for a further 24 hours. After, N/TERTs were cultured until confluent in FAD medium supplemented with 1 mg/ml puromycin before being replated and cultured again until confluent and then cryopreserved. Optimisation of Dox concentration was performed on the inducible NTC population and monitored by expression of the RFP transgene.

Flow cytometry

Transduced cells from monolayer culture were resuspended in PBS (10 × 10^6 cells/ml) and analyzed using the Becton Dickinson FACS Aria IIIu (BD Biosciences). RFP was detected on the Yellow-Green 582/12nm channel with forward scatter area and side scatter area detected on the blue laser with doublet discrimination determined by side scatter width.

Histological processing, embedding, and staining

On day 14, HSEs were removed from the Transwell inserts, gently rinsed with PBS, and fixed in 4% paraformaldehyde for 30 minutes. After 2 subsequent rinses in PBS, the HSEs were placed individually in tissue processor cassettes and stored in 70% ethanol prior to overnight dehydration in the Tissue-TEK processor (Sakura). HSEs were paraffin embedded and sectioned using the Leica RM2235 microtome (Leica Biosystems) into 8-μm-thick sections on glass SuperFrost slides.

For H&E staining, sections were incubated in 2 separate solutions of xylene for 3 minutes each. Afterward, slides were incubated in separate solutions of decreasing alcohol concentrations for 3 minutes each (100, 90, and 70%) followed by a further 3-minute incubation in ddH_2O. Slides were then sequentially submerged in haematoxylin for 3 minutes, rinsed, and then dipped in acid alcohol 5 times before being rinsed in running ddH2O for 5 minutes. Slides were then checked for the presence of stained nuclei under a light microscope and then submerged in eosin solution for 3 minutes before rinsing in running ddH2O for 5 minutes. For dehydration, sections were incubated in increasing solutions of ethanol for 3 minutes each (70, 90, and 100%) before transferring to the 2 separate xylene solutions for an additional 3 minutes. Finally, H&E-stained slides were mounted with coverslips using DPX Mountant

Table 1. List of the Product Numbers and Identification Codes for the Selected shRNA Constructs

Catalog Number	Source Clone ID	Vector	Gene	Gene Target Sequence	Lot Number
V3SH7669-225906623	V3IHSMCR_5844273	piSMART mCMV/TurboRFP	*CERS3*	GCAAAGAGA TGGATTGTTT	V20010204
V3SH7669-229884938	V3IHSMCR_9822588	piSMART mCMV/TurboRFP	*CERS3*	ACTTATGGG AGGTTTGGAA	V20010204
V3SH7669-229945592	V3IHSMCR_9883242	piSMART mCMV/TurboRFP	*CERS3*	GGATGGACG CAGACCTGTA	V20010204
VSC6571		mCMV/TurboRFP	Nontargeting control	N/A	05

Abbreviations: ID, identification; N/A, not applicable; shRNA, short hairpin RNA.

(Sigma-Aldrich) before imaging with the Nikon Eclipse 80i Stereology Microscope (Nikon).

For immunofluorescence, after deparaffinization, tissue sections were boiled at 100 °C for 15 minutes for antigen retrieval in pH 6 citrate buffer solution consisting of 10 mM sodium citrate tribasic and 1 M hydrogen chloride in ddH2O. Sections were then left to cool in the same buffer for 15 minutes. Tissues were permeabilized with 0.05% Triton-PBS solution for 5 minutes, followed by 2 subsequent PBS rinses before being placed in a blocking solution of 1% (w/v) fish gelatin (Sigma-Aldrich) and 2% (w/v) fetal bovine serum in PBS for 1 hour. Sections were then incubated with the selected primary antibodies diluted in blocking solution at 4 °C overnight. Primary antibodies included anti-keratin 14 (Sc-59724, Santa Cruz Technology, 1:100), anti-loricrin (ab85679, Abcam, 1:80), anti-TGM1 (HP040171, Atlas Antibodies, 1:200), and anti-tRFP (AB233, Evrogen, 1:1000). The next day, after rinsing with PBS, secondary antibodies diluted in blocking solution were applied to each section, covered, and then stored for 1 hour at room temperature. Secondary antibodies were antimouse Alexa Fluor 568 (A11004, Thermo Fisher Scientific, 1:1000) and antirabbit Alexa Fluor 488 (A11008, Thermo Fisher Scientific, 1:1000). After briefly rinsing with PBS, mounting medium with DAPI (104139, Abcam) was applied to each of the sections and coverslipped ready for imaging. Images were acquired using either the Leica DM4000 Epifluorescence or the Leica DM5000B Epifluorescence microscopes (Leica Microsystems). Normal human skin samples followed the same procedure.

For Nile red staining, samples were first deparaffinized as described previously. Then, a stock solution containing 0.05% Nile red in acetone was diluted to 2.5 μg/ml with 75:25 (v/v) glycerol-ddH2O, followed by rapid vortexing. Then, a drop of the glycerol-dye solution (20 μl) was applied to each tissue section and immediately covered with a coverslip. Slides were imaged 30 minutes later using the Leica DM4000 Epifluorescence microscope (Leica Microsystems). Exposure times were kept constant between conditions of the same experiments.

Image analysis

Fluorescence intensity of immunofluorescence and Nile red staining were analyzed with ImageJ by demarcating the epidermis and measuring the integrated intensity and mean gray values of the epidermis within the region of interest. For background subtraction, a region without tissue was measured using the same approach. Corrected total cell fluorescence was calculated by multiplying the region of interest area by the mean fluorescence of the background and subtracting this value from the integrated intensity. Epidermal thickness was analyzed using ImageJ and H&E images. The region of interest for the whole epidermis was drawn manually and divided by the length to determine the average thickness. Average thickness was calculated from 2 images per HSE and 3 technical replicates per experiment.

Western blotting

HSEs were removed from the Transwell inserts, and the epidermal layers were separated from the dermal matrix using a scalpel, rinsed with PBS, and placed into 1.5-ml microcentrifuge tubes. Tissues were then placed on ice and immersed in 125 μl of a supplemented RIPA buffer solution containing 1X protease inhibitor (Sigma-Aldrich). Samples were vortexed for 20 seconds, homogenized for 20 seconds, and sonicated for 5 minutes before being homogenized again for an additional 20 seconds. Samples were then centrifuged for 10 minutes at 4 °C at a rate of 9000*g*. Supernatants were collected and stored at −20 °C.

Equal amounts (20 μg) of protein were loaded onto the 4−20% Mini-PROTEAN TG Precast Protein running gels (Bio-Rad Laboratories) and run at 100 V for 1.5 hours. Membrane transfer was performed at 300 A for 1.5 hours onto a 0.45-μm nitrocellulose membrane, or the TransBlot Turbo Fast Transfer system (Bio-Rad Laboratories) was used for the transfer step. Membranes were blocked with 5% milk in Tris-buffered saline with 0.1% Tween. Membranes were incubated with the following primary antibodies: anti-CerS3 (HPA006092, Sigma-Aldrich, 1:1000) and anti-GAPDH (MAB374, Millipore, 1:5000) diluted in blocking solution overnight at 4 °C. Membranes were then washed 3 times in Tris-buffered saline with 0.1% Tween for 5 minutes and incubated for an additional 1 hour at room temperature with the following secondary antibodies: antimouse horseradish peroxidase (P0447, Dako, 1:15000) and antirabbit (P0448, Dako, 1:5000) diluted in 5% milk. Blots were washed again, 3 times for 5 minutes, and developed with Enhanced Chemiluminescence horseradish peroxidase substrate. Imaging was carried out on the ChemiDoc XRS imaging system (Bio-Rad Laboratories). Densitometry analysis of band intensity was performed using ImageJ.

RT-qPCR

RNA extraction was performed using the RNeasy Plus Mini Kit (Qiagen), following the instructions provided without the incorporation of either β-mercaptoethanol or dithiothreitol to the lysis RLT buffer. Samples were analyzed for RNA content and purity using the NanoDrop ND-1000 Spectrophotometer. For cDNA conversion, RNA samples were diluted to 1 μg total RNA for each sample, and the LunaScript RT SuperMix Kit (New England BioLabs) was used for reverse transcription.

Primers were designed using the University of California Santa Cruz Genome Browser (https://genome.ucsc.edu/) in parallel with

the National Centre for Biotechnology Information's Primer-BLAST tool (https://www.ncbi.nlm.nih.gov/tools/primer-blast/). The *CERS3* primer sequences were CCATCCAGTAGCTTCGCCTC and TCAGAGAGCAGCTTCCAACG. Primers were subsequently synthesized by Sigma-Aldrich at 100 μM concentrations in solution. GAPDH primers were synthesized by Eurofins (Eurofins Scientific). PCR reaction master mixes were made on ice using the 2× qPCRBIO Sybr Green Mix Hi-ROX kit (PCR Biosystems), with primers diluted to a 10-μM concentration. For each primer pair, non-cDNA triplicates were used as controls, and GAPDH was the housekeeper gene for all samples. Well plates were briefly spun prior to analysis on the StepOne Plu Real-Time PCR System (Applied Biosystems). Analysis was performed using the 2^{-DDCt} relative quantification method (Livak and Schmittgen, 2001).

Mass spectrometry

Lipid extraction was performed using a modified version of the Folch Extraction Method (Bligh and Dyer, 1959; Folch et al, 1951). Briefly, HSEs were washed twice in cold PBS before removal of the epidermal layers manually with a scalpel. Epidermal sheets were then placed in Agilent A-Line Amber Glass Vials and dissolved in a 2:1 chloroform/methanol solution at 4 °C overnight on a shaker. The supernatant was then removed, and the solution was filtered (0.4 μm pore size) and placed into fresh glass vials. Solutions were then dried with nitrogen gas and stored at −80 °C until analysis.

Lipid extracts were suspended in 200 μl of chloroform methanol (2:1 v/v). A total of 40 μl of a mixture of deuterated internal standards was added to the samples to control the intraday heterogeneity and to quantitate the relative abundance of detected lipids. The mixture included deuterated cholesterol-2,2,3,4,4,6-d6 (320 pmol); deuterated cholesterol sulphate sodium salt (160 pmol); hexadecanoic-9,9,10,10,11,11,12,12,13,13,14,14,15,15,16,16,16-d17 acid (640 pmol); N-palmitoyl-d31-D-erythro-sphingosine (8 pmol); glyceryl trihexadecanoate-d98 (160 pmol); 1-pentadecanoyl-2-oleyol(d7)-sn-glycerol (272 pmol); 25,26,26,26,27,27,27-heptadeuteriocholest-5-en-3ß-ol (9Z-octadecenoate) (243 pmol); 1-pentadecanoyl-2-oleoyl(d7)-sn-glycero-3-phosphocholine (212 pmol); 1-pentadecanoyl-2-oleoyl(d7)-sn-glycero-3-phosphoethanolamine (225 pmol); and N-oleoyl-D-erythro-sphingosylphosphorylcholine-d9 (217 pmol). The volume was filtered through the Captiva Vacuum (Agilent Technologies) with a pore size of 0.2 μm, and the filtrate was collected in graduated glass vials, dried under nitrogen flow, and suspended in 200 μl chloroform methanol (2:1 v/v).

For quantitative measurement of cholesterol, a gas chromatography-mass spectrometry analysis was performed. A total of 20 μl of the lipid extract was dried under nitrogen and then derivatized with 20 μl of 1% trimethylchlorosilane in pyridine. The reaction carried out at 60 °C for 60 minutes can produce the trimethylsilyl derivatives of most lipids. The gas chromatography-mass spectrometry instrument was an 8890 GC System combined with a 5977B Series MSD single-quadrupole (Agilent Technologies). Helium was used as the carrier gas; the flow rate was 1.2 ml/min. The analysis was conducted on the 30m × 0.250 mm (i.d.) × 0.25 μm film-thickness HP-5MS UI fused silica column (Agilent Technologies), chemically bound with a 5%-phenyl-methylpolysiloxane phase. The gas chromatography oven program was as follows: 80 °C at 0 minutes, 280 °C at 33 minutes, and 310 °C to final run time of 49 minutes. Samples were acquired in scan mode after EI ionization (Ludovici et al, 2018).

Triglycerides, diglycerides, and cholesteryl esters were detected in reversed-phase high-performance liquid chromatography under positive electrospray ionization ([+]ESI) conditions. Free fatty acids, ceramides, hexosylceramides, and cholesterol sulphate were analyzed under negative electrospray ionization ([−]ESI) conditions. To separate polar and hydrophilic compounds, hydrophilic interaction liquid chromatography was used. Phosphatidylcholines, ether-linked phosphatidyl-choline, sphingomyelins, phosphatidylethanolamines, and ether-linked phosphatidyl-ethanolamine were detected in hydrophilic interaction liquid chromatography (+)ESI mode. Reversed-phase high-performance liquid chromatography separation was conducted on an Agilent Technologies Infinity II 1260 series high-performance liquid chromatography system equipped with a degasser, a quaternary pump, an autosampler, and a column compartment. For the reversed-phase high-performance liquid chromatography separation, a Zorbax Eclipse Plus C18 column (2.1 × 50 mm, 1.8 μm particle size) (Agilent Technologies) was used. The column temperature was set at 60 °C, and the maximum operating pressure was 600 Bar/9000 psi. Cell extracts were eluted with a binary gradient of (A) MilliQ water (18.2 Ω) and (B) in methanol/isopropanol 80/20, and the flow rate was 0.3 ml/min. Mobile-phase additive was used to improve ionization efficiency. Hydrophilic interaction liquid chromatography separation was performed on a HALO HILIC column (Advanced Materials Technologies), 2.1 × 50 mm, 2.7 μm particle size, with maximum operating pressure at 600 Bar/9000 psi. The column temperature was set at 40 °C. The mobile phase consisted of (A) aqueous solutions of 5 mM ammonium formate in MilliQ water (18.2 Ω) and (C) acetonitrile. The mobile phase flow rate was 0.4 ml/min.

The high-performance liquid chromatography instrument was connected by an ESI Dual Agilent Jet Stream interface with an Agilent Technologies 6545 Quadrupole Time of Flight as mass spectrometer. Nitrogen was used as a gas for both the nebulization and desolvation processes. The ion source gas temperature was 200 °C with a flow rate of 12 l/min; the nebulizer pressure was 40 psi. Sheath gas temperature was set at 350 °C; sheath gas flow rate was 12 l/min. The fragmentor voltage parameter was 120 V, and the skimmer was 40 V. Data were collected in all ion tandem mass spectrometry modes, at 0, 20, 40 V of collision energies. The m/z range for mass spectrometry and tandem mass spectrometry was 59−1700 at a mass resolving power of 40,000. Internal mass calibration for accurate mass measurement used 2 reference ions: m/z 121.0509 and m/z 922.0098 (+)ESI and m/z 119.0363 and m/z 940.0015 (−)ESI. For analysis, all data were derived by normalizing the response of the individual lipid by the response of the same-class labeled internal standard (eg, free fatty acids vs deuterated palmitic acid, cholesterol vs deuterated cholesterol, etc) and multiplied by the iSTD pmole. Resulting pmoles were normalized by total nmole amount of each sample.

Statistical analysis

All data represent the mean of 3 independent experiments and were primarily analyzed by 1- or 2-way ANOVA and Tukey's multiple comparisons test. Changes in individual lipid species (Figure 4c and d) were analyzed by unpaired *t*-tests between the NTC + Dox-treated groups and either sh1 + Dox or sh2 + Dox groups. Differences were considered statistically significant with $P < .05$. All statistical analysis was performed using Prism (GraphPad Software), and additional graphing (volcano plots) were conducted using R Statistical Software (v2023.06.1+524 "Mountain Hydrangea").

ETHICS STATEMENT

Collection of redundant human skin from plastic surgery procedures was approved by the NHS London Research Committee (study reference number LREC 08/H0704/65). All participants provided informed written consent prior to tissue collection.

DATA AVAILABILITY STATEMENT

Processed lipidomic data are provided as a supplementary dataset. All other raw or processed data will be made available on request.

ORCIDs

Durotimi O. Dina: http://orcid.org/0009-0009-8227-6126
Miriam Maiellaro: http://orcid.org/0000-0003-3298-4780
Emanuela Camera: http://orcid.org/0000-0001-6633-0449
John T. Connelly: http://orcid.org/0000-0002-5955-8848

CONFLICT OF INTEREST

The authors state no conflict of interest.

ACKNOWLEDGMENTS

This work was funded by a PhD studentship from the Biotechnology and Biological Sciences Research Council London Interdisciplinary Doctoral Programme. We thank Matthew Caley and Edel O'Toole for their advice and guidance on retroviral transductions and human skin equivalent methods.

AUTHOR CONTRIBUTIONS

Conceptualization: JTC; Formal Analysis: DOD, MM, HK, EC, JTC; Funding Acquisition: JTC; Investigation: DOD, MM, HK; Supervision: JTC; Writing — Original Draft Preparation: DOD, JTC; Writing — Review and Editing: DOD, EC, JTC

DECLARATION OF GENERATIVE ARTIFICIAL INTELLIGENCE (AI) OR LARGE LANGUAGE MODELS (LLMs)

The author(s) did not use AI/LLM in any part of the research process and/or manuscript preparation.

SUPPLEMENTARY MATERIAL

Supplementary material is linked to the online version of the paper at www.jidonline.org, and at https://doi.org/10.1016/j.xjidi.2025.100383.

REFERENCES

Akiyama M. Corneocyte lipid envelope (CLE), the key structure for skin barrier function and ichthyosis pathogenesis. J Dermatol Sci 2017;88:3–9.

Baron U, Bujard H. Tet repressor-based system for regulated gene expression in eukaryotic cells: principles and advances. Methods Enzymol 2000;327:401–21.

Behne M, Uchida Y, Seki T, de Montellano PO, Elias PM, Holleran WM. Omega-hydroxyceramides are required for corneocyte lipid envelope (CLE) formation and normal epidermal permeability barrier function. J Invest Dermatol 2000;114:185–92.

Bligh EG, Dyer WJ. A rapid method of total lipid extraction and purification. Can J Biochem Physiol 1959;37:911–7.

Bouwstra J, Pilgram G, Gooris G, Koerten H, Ponec M. New aspects of the skin barrier organization. Skin Pharmacol Appl Skin Physiol 2001;14(Suppl 1):52–62.

Bouwstra JA, Dubbelaar FE, Gooris GS, Ponec M. The lipid organisation in the skin barrier. Acta Derm Venereol Suppl (Stockh) 2000;208:23–30.

Bouwstra JA, Gooris GS, Dubbelaar FE, Ponec M. Phase behavior of stratum corneum lipid mixtures based on human ceramides: the role of natural and synthetic ceramide 1. J Invest Dermatol 2002;118:606–17.

Bouwstra JA, Gooris GS, Dubbelaar FE, Weerheim AM, Ijzerman AP, Ponec M. Role of ceramide 1 in the molecular organization of the stratum corneum lipids. J Lipid Res 1998;39:186–96.

Breiden B, Sandhoff K. The role of sphingolipid metabolism in cutaneous permeability barrier formation. Biochim Biophys Acta 2014;1841:441–52.

Coderch L, López O, De La Maza A, Parra JL. Ceramides and skin function. Am J Clin Dermatol 2003;4:107–29.

Danso M, Boiten W, Van Drongelen V, Gmelig Meijling K, Gooris G, El Ghalbzouri A, et al. Altered expression of epidermal lipid Bio-Synthesis enzymes in atopic dermatitis skin is accompanied by changes in stratum corneum lipid composition. J Dermatol Sci 2017;88:57–66.

Danso MO, Van Drongelen V, Mulder A, Gooris G, Van Smeden J, El Ghalbzouri A, et al. Exploring the potentials of nurture: 2(nd) and 3(rd) generation explant human skin equivalents. J Dermatol Sci 2015;77:102–9.

Derr K, Zou J, Luo K, Song MJ, Sittampalam GS, Zhou C, et al. Fully three-dimensional bioprinted skin equivalent constructs with validated morphology and barrier function. Tissue Eng Part C Methods 2019;25:334–43.

Dickson MA, Hahn WC, Ino Y, Ronfard V, Wu JY, Weinberg RA, et al. Human keratinocytes that express hTERT and also bypass a p16(INK4a)-enforced mechanism that limits life span become immortal yet retain normal growth and differentiation characteristics. Mol Cell Biol 2000;20:1436–47.

Eckl KM, Tidhar R, Thiele H, Oji V, Hausser I, Brodesser S, et al. Impaired epidermal ceramide synthesis causes autosomal recessive congenital ichthyosis and reveals the importance of ceramide acyl chain length. J Invest Dermatol 2013;133:2202–11.

Elias PM, Gruber R, Crumrine D, Menon G, Williams ML, Wakefield JS, et al. Formation and functions of the corneocyte lipid envelope (CLE). Biochim Biophys Acta 2014;1841:314–8.

Elias PM, Williams ML, Maloney ME, Bonifas JA, Brown BE, Grayson S, et al. Stratum corneum lipids in disorders of cornification. Steroid sulfatase and cholesterol sulfate in normal desquamation and the pathogenesis of recessive X-linked ichthyosis. J Clin Invest 1984;74:1414–21.

Enjalbert F, Dewan P, Caley MP, Jones EM, Morse MA, Kelsell DP, et al. 3D model of harlequin ichthyosis reveals inflammatory therapeutic targets. J Clin Invest 2020;130:4798–810.

Feingold KR, Elias PM. Role of lipids in the formation and maintenance of the cutaneous permeability barrier. Biochim Biophys Acta 2014;1841:280–94.

Folch J, Ascoli I, Lees M, Meath JA, LeBaron N. Preparation of lipide extracts from brain tissue. J Biol Chem 1951;191:833–41.

Fowler SD, Greenspan P. Application of Nile red, a fluorescent hydrophobic probe, for the detection of neutral lipid deposits in tissue sections: comparison with oil red O. J Histochem Cytochem 1985;33:833–6.

Imokawa G, Abe A, Jin K, Higaki Y, Kawashima M, Hidano A. Decreased level of ceramides in stratum corneum of atopic dermatitis: an etiologic factor in atopic dry skin? J Invest Dermatol 1991;96:523–6.

Ishikawa J, Narita H, Kondo N, Hotta M, Takagi Y, Masukawa Y, et al. Changes in the ceramide profile of atopic dermatitis patients. J Invest Dermatol 2010;130:2511–4.

Janssens M, Van Smeden J, Gooris GS, Bras W, Portale G, Caspers PJ, et al. Increase in short-chain ceramides correlates with an altered lipid organization and decreased barrier function in atopic eczema patients. J Lipid Res 2012;53:2755–66.

Jennemann R, Rabionet M, Gorgas K, Epstein S, Dalpke A, Rothermel U, et al. Loss of ceramide synthase 3 causes lethal skin barrier disruption. Hum Mol Genet 2012;21:586–608.

Kawana M, Miyamoto M, Ohno Y, Kihara A. Comparative profiling and comprehensive quantification of stratum corneum ceramides in humans and mice by LC/MS/MS. J Lipid Res 2020;61:884–95.

Kendall AC, Kiezel-Tsugunova M, Brownbridge LC, Harwood JL, Nicolaou A. Lipid functions in skin: differential effects of n-3 polyunsaturated fatty acids on cutaneous ceramides, in a human skin organ culture model. Biochim Biophys Acta Biomembr 2017;1859:1679–89.

Kihara A. Synthesis and degradation pathways, functions, and pathology of ceramides and epidermal acylceramides. Prog Lipid Res 2016;63:50–69.

Kováčik A, Roh J, Vávrová K. The chemistry and biology of 6-hydroxyceramide, the youngest member of the human sphingolipid family. Chembiochem 2014;15:1555–62.

Livak KJ, Schmittgen TD. Analysis of relative gene expression data using real-time quantitative PCR and the 2(-Delta Chimbote C(T)) method. Methods 2001;25:402–8.

Loew R, Heinz N, Hampf M, Bujard H, Gossen M. Improved Tet-responsive promoters with minimized background expression. BMC Biotechnol 2010;10:81.

Ludovici M, Kozul N, Materazzi S, Risoluti R, Picardo M, Camera E. Influence of the sebaceous gland density on the stratum corneum lipidome. Sci Rep 2018;8:11500.

Mieremet A, Boiten W, Van Dijk R, Gooris G, Overkleeft HS, Aerts JMFG, et al. Unravelling effects of relative humidity on lipid barrier formation in human skin equivalents. Arch Dermatol Res 2019;311:679–89.

Mizutani Y, Mitsutake S, Tsuji K, Kihara A, Igarashi Y. Ceramide biosynthesis in keratinocyte and its role in skin function. Biochimie 2009;91:784–90.

Mizutani Y, Sun H, Ohno Y, Sassa T, Wakashima T, Obara M, et al. Cooperative synthesis of ultra long-chain fatty acid and ceramide during keratinocyte differentiation. PLOS One 2013;8:e67317.

Mullen TD, Hannun YA, Obeid LM. Ceramide synthases at the centre of sphingolipid metabolism and biology. Biochem J 2012;441:789–802.

Nemes Z, Steinert PM. Bricks and mortar of the epidermal barrier. Exp Mol Med 1999;31:5–19.

Oji V, Tadini G, Akiyama M, Blanchet Bardon C, Bodemer C, Bourrat E, et al. Revised nomenclature and classification of inherited ichthyoses: results of the first ichthyosis Consensus Conference in Sorèze 2009. J Am Acad Dermatol 2010;63:607–41.

Rabionet M, Gorgas K, Sandhoff R. Ceramide synthesis in the epidermis. Biochim Biophys Acta 2014;1841:422–34.

Radner FP, Marrakchi S, Kirchmeier P, Kim GJ, Ribierre F, Kamoun B, et al. Mutations in CERS3 cause autosomal recessive congenital ichthyosis in humans. PLoS Genet 2013;9:1–11.

Reijnders CM, van Lier A, Roffel S, Kramer D, Scheper RJ, Gibbs S. Development of a full-thickness human skin equivalent in vitro model derived from TERT-immortalized keratinocytes and fibroblasts. Tissue Eng Part A 2015;21:2448–59.

Sahle FF, Gebre-Mariam T, Dobner B, Wohlrab J, Neubert RH. Skin diseases associated with the depletion of stratum corneum lipids and stratum corneum lipid substitution therapy. Skin Pharmacol Physiol 2015;28:42–55.

Sarmin AM, Connelly JT. Fabrication of human skin equivalents using decellularized extracellular matrix. Curr Protoc 2022;2:e393.

Schreiner V, Gooris GS, Pfeiffer S, Lanzendörfer G, Wenck H, Diembeck W, et al. Barrier characteristics of different human skin types investigated with X-ray diffraction, lipid analysis, and electron microscopy imaging. J Invest Dermatol 2000;114:654–60.

Shen CP, Zhao MT, Jia ZX, Zhang JL, Jiao L, Ma L. Skin ceramide profile in children with atopic dermatitis. Dermatitis 2018;29:219–22.

Sheu HM, Tsai JC, Lin TK, Wong TW, Lee JY. Modified Nile red staining method for improved visualization of neutral lipid depositions in stratum corneum. J Formos Med Assoc 2003;102:656–60.

Suzuki M, Ohno Y, Kihara A. Whole picture of human stratum corneum ceramides, including the chain-length diversity of long-chain bases. J Lipid Res 2022;63:100235.

Thakoersing VS, Van Smeden J, Mulder AA, Vreeken RJ, El Ghalbzouri A, Bouwstra JA. Increased presence of monounsaturated fatty acids in the stratum corneum of human skin equivalents. J Invest Dermatol 2013;133:59–67.

t'Kindt R, Jorge L, Dumont E, Couturon P, David F, Sandra P, et al. Profiling and characterizing skin ceramides using reversed-phase liquid chromatography-quadrupole time-of-flight mass spectrometry. Anal Chem 2012;84:403–11.

Van Drongelen V, Danso MO, Mulder A, Mieremet A, Van Smeden J, Bouwstra JA, et al. Barrier properties of an N/TERT-based human skin equivalent. Tissue Eng Part A 2014;20:3041–9.

Van Smeden J, Janssens M, Gooris GS, Bouwstra JA. The important role of stratum corneum lipids for the cutaneous barrier function. Biochim Biophys Acta 2014;1841:295–313.

Wegner MS, Schiffmann S, Parnham MJ, Geisslinger G, Grösch S. The enigma of ceramide synthase regulation in mammalian cells. Prog Lipid Res 2016;63:93–119.

Wertz PW, Swartzendruber DC, Kitko DJ, Madison KC, Downing DT. The role of the corneocyte lipid envelopes in cohesion of the stratum corneum. J Invest Dermatol 1989;93:169–72.

Yamamoto M, Sassa T, Kyono Y, Uemura H, Kugo M, Hayashi H, et al. Comprehensive stratum corneum ceramide profiling reveals reduced acylceramides in ichthyosis patient with CERS3 mutations. J Dermatol 2021;48:447–56.

Yokose U, Ishikawa J, Morokuma Y, Naoe A, Inoue Y, Yasuda Y, et al. The ceramide [NP]/[NS] ratio in the stratum corneum is a potential marker for skin properties and epidermal differentiation. BMC Dermatol 2020;20:6.

Zhou X, Vink M, Klaver B, Berkhout B, Das AT. Optimization of the Tet-On system for regulated gene expression through viral evolution. Gene Ther 2006;13:1382–90.